ELSEVIER

International Journal of Heat and Fluid Flow 23 (2002) 346–358

International Journal of HEAT AND FLUID FLOW

www.elsevier.com/locate/ijhff

Laminar and turbulent Rayleigh–Bénard convection in a perfectly conducting cubical cavity ☆

J. Pallares *, I. Cuesta, F.X. Grau

Department of Mechanical Engineering, Universitat Rovira i Virgili, Avinguda dels Països Catalans 26, 43007 Tarragona, Spain

Abstract

This paper discusses flow structures and heat transfer rates generated by Rayleigh–Bénard convective motions of a Boussinesq fluid with a Prandtl number of 0.7 in a perfectly conducting cubical cavity. Complete numerical simulations of laminar flows were conducted in the range of Rayleigh numbers $7 \times 10^3 \leqslant Ra \leqslant 10^5$. The large-eddy simulation (LES) technique was used for the simulations at two high Rayleigh numbers ($Ra = 10^6$ and 10^8). LES were carried out using a second-order accurate finite volume code with a dynamic localized one-equation subgrid-scale (SGS) model with constant SGS Prandtl number. In the laminar regime, two single roll structures and a four-roll structure in which the axis of each roll is perpendicular to one sidewall were found to be stable. LES of Rayleigh–Bénard convection in an infinite fluid layer were initially carried out and results were seen to be in agreement with direct numerical simulations (DNS) reported in the literature. At $Ra = 10^6$ and 10^8, the instantaneous velocity and temperature fields present strong fluctuations with respect to the time-averaged flow field. The confining effect of the conductive lateral walls of the cavity generates, in the unsteady flows at $Ra = 10^6$ and 10^8, persistent vertical currents near these walls. The recirculation of these ascending and descending flows towards the central region of the cavity produces large-scale organized rolling motions, which imprint the topology of the time-averaged flow field in form of two vortex ring structures located near the horizontal walls.

Keywords: Rayleigh–Bénard convection; Cubical cavity; Large-eddy simulation; Turbulent natural convection

1. Introduction

Rayleigh–Bénard convection is a type of natural convection that is produced by an unstable vertical density stratification in a bounded horizontal fluid layer. It is of considerable scientific and engineering importance, and is related to some of the flow phenomena in problems of thermal comfort in buildings, crystal growth, solar collectors and the refrigeration of electronic circuit boards. It has been extensively studied inside rectangular cavities because of the geometrical simplicity of the boundary conditions. The flow in these cavities is governed by a set of coupled non-linear partial differential equations. It is particularly suitable for studying the transition to turbulence because, under certain conditions and when the Rayleigh number is increased, the increasing flow complexity takes the form of discrete flow transitions that can be studied individually. A complete review on Rayleigh–Bénard convection can be found in Koschmieder (1993).

Considerable efforts have been made to predict the heat transfer processes produced at the walls by the convective motions in the Rayleigh–Bénard flows. The Nusselt number ($Nu = hL/k$), which characterizes the heat transfer rates at the walls, depends on the non-dimensional parameters involved in the transport equations, the Rayleigh number ($Ra = g\beta\Delta TL^3/\nu\alpha$), the Prandtl number ($Pr = \nu/\alpha$), and the aspect ratios of the enclosure. The type of thermal boundary conditions applied at the walls of the enclosure and the type of flow structure, for a given set of non-dimensional parameters, may have a considerable effect on the Nusselt number.

Natural convection in side-heated cubical cavities has been extensively studied using numerical simulations and experiments (Leong et al., 1999). The flow in this system invariably occurs with ascending/descending flows near

☆ This paper is a revised and expanded version of a paper presented at CHT'01, the Second International Symposium on Advances in Computational Heat Transfer (Palm Cove, Qld., Australia, 20–25 May 2001), the proceedings of which were published by Begell House, Inc.

* Corresponding author. Tel.: +34-977-559-682; fax: +34-977-559-691.

E-mail address: pallares@etseq.urv.es (J. Pallares).

0142-727X/02/$ - see front matter
PII: S0142-727X(02)00182-0

Nomenclature

C	subgrid-scale (SGS) model coefficient
f	frequency (s^{-1})
g	gravitational acceleration ($m\,s^{-2}$)
h	convective heat transfer coefficient ($W\,m^{-2}\,K^{-1}$)
h_j	SGS heat flux ($m\,K\,s^{-1}$)
K	kinetic energy ($J\,kg^{-1}$)
k	thermal conductivity ($W\,m^{-1}\,K^{-1}$)
L	height of the cavity (m)
N	number of grid points
Nu	Nusselt number, hL/k
p	pressure (Pa)
Pr	Prandtl number, v/α
q	heat flux ($W\,m^{-2}$)
Ra	Rayleigh number, $g\beta\Delta TL^3/v\alpha$
S	area (m^2)
S_{ij}	strain tensor (s^{-1})
T	temperature (K)
t	time (s)
u, v, w	velocity components ($m\,s^{-1}$)
x, y, z	cartesian coordinates (m)

Greeks

Δ	increment
α	thermal diffusivity ($m^2\,s^{-1}$)
β	thermal expansion coefficient (K^{-1})
δ_{ij}	Kronecker delta
λ_2	second largest eigenvalue of the velocity gradient tensor
v	kinematic viscosity ($m^2\,s^{-1}$)
τ_{ij}	SGS stress tensor ($N\,m^{-2}$)

Superscripts and subscripts

’	fluctuation
$*$	dimensional quantity
C	cold wall
H	hot wall
0	reference value
rms	root mean square
s	sampling
SGS	subgrid-scale
V	volume averaged
w	wall

the heated/cooled vertical wall. The number of stable flow patterns or flow structures that develop increases when the imposed temperature gradient is parallel to the gravity vector and the parallelepiped enclosure tends to the cubical geometry with no preferred horizontal direction. Pallares et al. (1999) and Pallares et al. (2001) describe numerical simulations and experimentally measured Rayleigh–Bénard flows at a high Prandtl number ($Pr = 130$) in a cubical cavity with perfectly insulated or perfectly conducting sidewalls (i.e. linear temperature distribution on the lateral walls). They identified three different single roll structures—two with the rotation axis perpendicular to two opposite vertical walls and one with the rotation axis perpendicular to two diagonally opposite vertical edges—a toroidal roll and two four-roll structures. Fig. 1 shows the symmetry elements for these flow structures in the horizontal midplane and the nomenclature proposed by Pallares et al. (2001). It should be noted that because of the symmetry of the problem, the symmetry elements and the ascending and descending regions shown in Fig. 1 can be rotated 90°, 180° or 270° with respect to the vertical symmetry axis of the cubical cavity. The toroidal roll can also be obtained with the descending central current and ascending currents near the sidewalls.

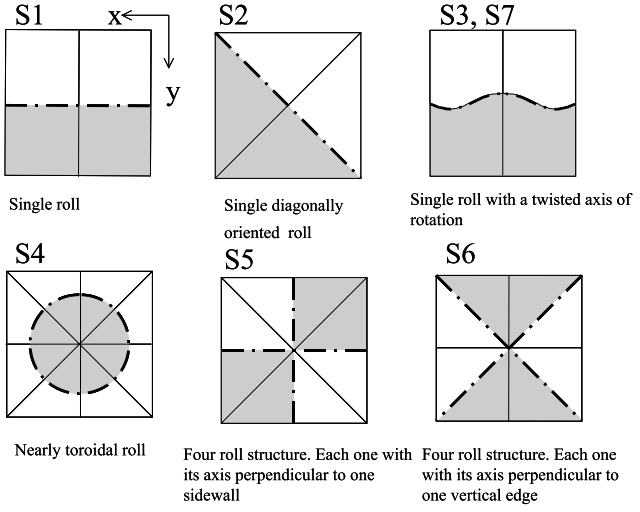

Fig. 1. Symmetry elements of the Rayleigh–Bénard convective structures in the horizontal midplane of a cubical cavity according to Pallares et al. (2001). (▩) Ascending fluid, (□) descending fluid, (-·-·-·) roll axis, (—) symmetry plane.

Recently, Leong et al. (1999) reported experimentally measured average Nusselt numbers produced by Rayleigh–Bénard flows ($10^4 \leqslant Ra \leqslant 10^8$) at the bottom hot wall of a perfectly conducting cubical cavity at $Pr = 0.7$. However, they did not report any direct experimental information about the flow topology. They inferred the flow structure at $Ra = 10^5$ by carrying out numerical simulations and by comparing the values of the measured and computed average Nusselt numbers. The numerical simulation was conducted only in one half of the cavity by imposing symmetry boundary conditions for velocity and temperature in the vertical midplane.

The present study analyses numerically the laminar and turbulent Rayleigh–Bénard flows at $Pr = 0.7$ in a

perfectly conducting cubical cavity to determine the flow structures that may develop in the range of Rayleigh numbers covered by the experiments of Leong et al. (1999). The computations were performed without any a priori assumption about the symmetry of the flow structure. This is an important feature because different steady flow structures with different symmetry elements (see Fig. 1) may lead to different heat transfer rates (Pallares et al., 1999). It should be noted that the imposition of symmetry conditions on an unsteady structure could inhibit or excite certain natural wavelengths of the flow.

2. Model

The physical model of the cubical cavity is shown in Fig. 2. The six walls of the cavity are solid, immobile and perfectly conducting. The top and the bottom plates are maintained at uniform and constant temperatures. A vertical linear temperature distribution is imposed at the sidewalls. According to the Boussinesq approximation, the physical properties of the fluid ($Pr = 0.7$) are assumed to be constant. Only a linear variation of density with temperature is taken into account in the buoyancy term of the momentum equation corresponding to the vertical direction. The continuity equation, the three-dimensional Navier–Stokes equations and the thermal energy equation in terms of non-dimensional variables are,

$$\frac{\partial u_i}{\partial x_i} = 0, \tag{1}$$

$$\frac{\partial u_i}{\partial t} + \frac{\partial u_j u_i}{\partial x_j} = -\frac{\partial p}{\partial x_i} + \sqrt{\frac{Pr}{Ra}}\frac{\partial^2 u_i}{\partial x_j \partial x_j} + \delta_{i3} T \tag{2}$$

and

$$\frac{\partial T}{\partial t} + \frac{\partial u_j T}{\partial x_j} = \frac{1}{\sqrt{Pr\,Ra}}\frac{\partial^2 T}{\partial x_j \partial x_j} \tag{3}$$

respectively. The scales used to obtain the non-dimensional variables are the height of the cavity (L) and the velocity scale, $u^* = (g\beta\Delta T L)^{1/2}$. Pressure was scaled with ρu^{*2} and the non-dimensional temperature, T, is defined as $T = (T^* - T_0)/\Delta T$ where T_0 is the mean temperature, $T_0 = (T_H + T_C)/2$, and ΔT is the temperature difference, $\Delta T = T_H - T_C$. The non-slip boundary condition for velocity is applied at the six walls. Constant temperature boundary conditions are used at the hot bottom wall ($T_H = 1/2$) and at the top wall ($T_C = -1/2$) and a fixed linear temperature profile, $T = -z + 1/2$, is imposed at the four perfectly conducting sidewalls.

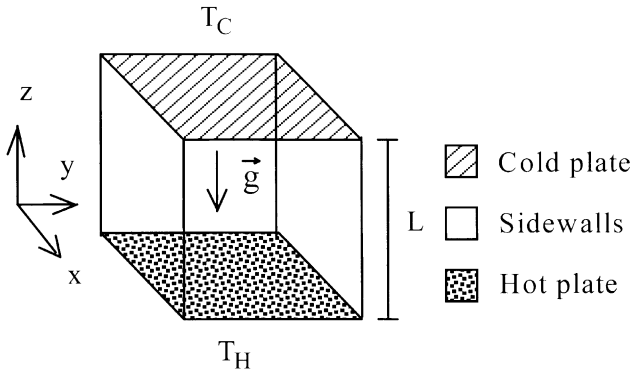

Fig. 2. Physical model and coordinate system.

Eqs. (1)–(3) and the corresponding boundary conditions have been solved numerically by the second order accuracy control volume code 3DINAMICS. The diffusive fluxes are discretized in a staggered grid using a central scheme. The second order QUICK and central formulations can be optionally selected to compute the convective fluxes. The code can perform the time-marching procedure with a semi-implicit ADI method or with an explicit Adams–Bashforth scheme. The coupling between the pressure and velocity field was computed using a predictor–corrector scheme involving a Poisson equation that was solved with the conjugate gradient method. The complete mathematical formulations and a detailed description of the numerical methods can be found in Cuesta (1993). In the present study, the QUICK and the semi-implicit formulations have been used in the computations in the cubical cavity at $Ra \leqslant 10^5$. In this range of Rayleigh numbers and for the Prandtl number considered ($Pr = 0.7$) the flow is laminar. The non-dimensional time step $\Delta t = \Delta t^* u_0^*/L = 2$ used at $Ra = 6 \times 10^4$ for which the flow is oscillatory is small enough in comparison with the period of oscillation of the flow ($1/f = 100$). Uniform grids of 41^3 nodes have been used for the low Rayleigh number simulations ($Ra \leqslant 10^5$). The adequacy of the code for describing these flows is shown in Pallares et al. (2001) where numerical velocity distributions of the different flow structures at $Ra \leqslant 8 \times 10^4$ and $Pr = 130$, computed using the same grid resolution, were compared successfully with the corresponding PIV measured distributions. At $Ra = 8 \times 10^4$ and $Pr = 130$ the difference on average Nusselt numbers using uniform grids of 41^3 and 81^3 nodes was 2.5%.

The LES technique has been used for the computations at $Ra = 10^6$ and 10^8. LES is based on the decomposition of the flow quantities into a large-scale component, which is defined by the filtering operation and is resolved by the grid, and a subgrid-scale (SGS) component that has to be modeled (Germano et al., 1991). The filtering operation, applied to Eqs. (1)–(3), generates additional terms on the right-hand side of Eq. (2) ($-\partial\tau_{ij}/\partial x_j$) and on the right-hand side of Eq. (3) ($-\partial h_j/\partial x_j$) which are responsible of the SGS contributions to the instantaneous large-scale momentum and thermal energy budgets, respectively. The anisotropic part of the SGS tensor is modeled in alignment with

the resolved local strain rate tensor ($\tau_{ij} - \delta_{ij}\tau_{kk}/3 = -2\nu_{SGS}S_{ij}$). By analogy to τ_{ij}, the SGS heat fluxes are modeled using a gradient–diffusion hypothesis ($h_j = -\alpha_{SGS}\partial T/\partial x_j$). The SGS diffusivity of momentum (ν_{SGS}) was computed following the localized one-equation dynamic SGS model proposed by Kim and Menon (1997). In this model the SGS viscosity is computed as

$$\nu_{SGS} = C\Delta(K_{SGS})^{1/2}. \quad (4)$$

Eq. (4) indicates that the local SGS viscosity is assumed to be proportional to the product of the SGS length-scale, imposed by the local grid resolution ($\Delta = \{\Delta x\ \Delta y\ \Delta z\}^{1/3}$), and to the SGS velocity scale, given by the square-root of the local SGS kinetic energy (K_{SGS}). In Eq. (4), the local K_{SGS} is computed dynamically by solving its transport equation in which the turbulent transport and dissipation terms are modeled. The buoyancy production term in this equation is computed from the resolved temperature field. The local model coefficient, C, is determined using the dynamic procedure (Germano et al., 1991). The complete formulation of the SGS model can be found in Kim and Menon (1997).

A constant SGS Prandtl number ($Pr_{SGS} = \nu_{SGS}/\alpha_{SGS} = 0.4$) was used to compute the SGS heat fluxes (i.e. $h_j = -\{\nu_{SGS}/0.4\}\partial T/\partial x_j$) as in previous LES of turbulent Rayleigh–Bénard flows which had not shown significant differences in average quantities using a constant Pr_{SGS} or by computing it dynamically (Peng and Davidson, 1998).

LES at $Ra = 10^6$ and 10^8 were performed using the central scheme for the convective fluxes because the upwind schemes are known to introduce significant numerical dissipation in the resolved flow structures (Mittal and Moin, 1997). LES of turbulent flows require small time-steps to capture the unsteadiness of the grid-resolved scales. Consequently, the explicit Adams–Bashforth scheme with time steps of $\Delta t = 0.001$ ($Ra = 10^6$) and $\Delta t = 0.002$ ($Ra = 10^8$) have been used in the present LES. Table 1 shows the computational details of the LES at $Ra = 10^6$ and 10^8. The CPU times were 13 ($Ra = 10^6$) and 40 ($Ra = 10^8$) seconds per time step in an AMD-K7 at 1.2 GHz.

3. Validation

Before the discussion of the simulations of the flow in a cubical cavity and the comparison with the experiments of Leong et al. (1999), it is necessary to establish the validity of the code in predicting turbulent RB flows. To do so, the well-documented turbulent Rayleigh–Bénard flow in an infinite fluid layer has been chosen as a benchmark case. These simulations were conducted at $Ra = 6.3 \times 10^5$ and $Pr = 0.7$, in a computational box of aspect ratios $Lx/L = 6$, $Ly/L = 6$, $Lz/L = 1$ using the centered scheme for the convective terms and the explicit time-marching procedure. A coarse-grid simulation at $Ra = 6.3 \times 10^5$ was carried out using the conductive state (i.e. linear temperature distribution and zero velocity field) as initial conditions. When the turbulent flow was fully developed, an instantaneous flow field was interpolated in a refined grid. The interpolated data was used as initial conditions for the computations at the new grid resolution. It should be noted that the data sampling procedure to obtain the statistics of the flow was not started until the flow was fully developed. The mean flow quantities were averaged along the homogeneous x- and y-directions, typically during 4500 time steps (i.e. 45 non-dimensional time units). Table 2 summarizes the computational details of the DNS carried out by Kerr (1996) and Woerner (1994) and the present coarse-grid DNS (CDNS) using $61 \times 81 \times 81$ (Mesh A), $41 \times 81 \times 81$ (Mesh B) and $31 \times 81 \times 81$

Table 1
Computational details of LES of Rayleigh–Bénard convection ($Pr = 0.7$) in a perfectly conducting cubical cavity

Ra	N_x	N_y	N_z	$\Delta x_{min}\ \Delta y_{min}$	$\Delta x_{max}\ \Delta y_{max}$	Δz_{min}	Δz_{max}	Δt
10^6	61	61	61	3.6×10^{-3}	3.6×10^{-2}	3.6×10^{-3}	3.6×10^{-2}	10^{-3}
10^8	81	81	101	2×10^{-3}	2.8×10^{-2}	10^{-3}	2.8×10^{-2}	2×10^{-3}

Table 2
Computational characteristics of DNS of turbulent Rayleigh–Bénard convection in an infinite fluid ($Pr = 0.7$) layer

	Ra	L_x	L_y	L_z	$N_x = N_y$	$\Delta_x = \Delta y$	N_z	Δz_{min}	Δz_{max}	Nu
Woerner (1994)	6.3×10^5	7.9	7.9	1	200	0.0396	49	0.005	0.0369	7.27
Kerr (1996)	5×10^5	6	6	1	96	0.0625	48	0.002	0.0480	7.46[a]
Present study	6.3×10^5	6	6	1	81	0.0759	61	0.004	0.0302	7.6
							41	0.008	0.0377	7.7
							31	0.008	0.0734	7.7

[a] This value of Nu, which corresponds to $Ra = 6.3 \times 10^5$, has been calculated by a least squares fit ($Nu = 0.186Ra^{0.276}$) of the results of Kerr (1996) in the range $5 \times 10^4 \leqslant Ra \leqslant 2 \times 10^7$.

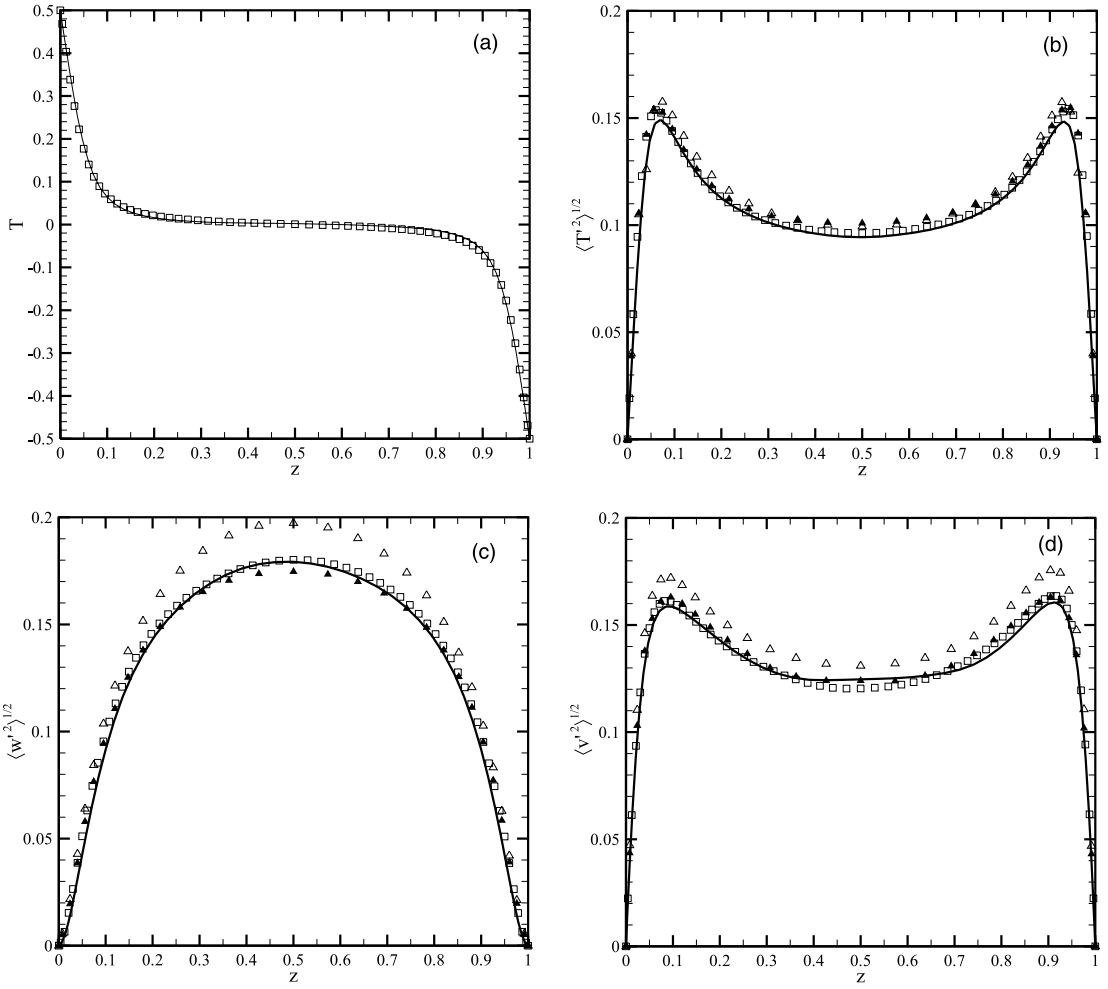

Fig. 3. Mean temperature (a) and fluctuation intensities (b, c and d) profiles in Rayleigh–Bénard convection in an infinite fluid layer at $Ra = 6.3 \times 10^5$ and $Pr = 0.7$. (—) DNS results of Woerner (1994). (□) CDNS Mesh A ($61 \times 81 \times 81$). (△) CDNS Mesh C ($31 \times 81 \times 81$). (▲) LES Mesh C ($31 \times 81 \times 81$).

(Mesh C) grid nodes. Uniform grid distributions were used along the homogeneous x- and y-directions in which periodic boundary conditions were imposed. The grid along the z-direction was stretched near the walls ($z = 0$ and 1) where the non-slip and constant temperature boundary conditions were used. It can be seen in Table 2 that the present predictions of the time averaged Nusselt number are about 5% and 2% higher than the values given by Woerner (1994) and Kerr (1996), respectively. This can be probably attributed to the insufficient grid resolution of the present simulations along the x- and y-directions (see Table 2). Large-eddy simulations (LESs) using Mesh B and C predict the same values of the time-averaged Nusselt numbers shown in Table 2, indicating that for the present computational conditions the SGS model has no influence on the averaged wall heat flux. Fig. 3 shows the vertical profiles of the averaged temperature (Fig. 3(a)) and the rms of the temperature (Fig. 3(b)) and velocity fluctuations (Fig. 3(c) and (d)) together with the corresponding predictions of Woerner (1994). It can be seen in Fig. 3(a) that the average temperature profile is well reproduced by the CDNS using Mesh A. An undistinguishable agreement is found when comparing the average temperature profiles of the LES, not shown in Fig. 3(a), and CDNS using Mesh B or C. The benefits of the SGS model are more evident when comparing the profiles of the velocity fluctuations in Fig. 3(c) and (d) using Mesh C. The CDNS (Mesh C) without any SGS model clearly overpredicts, by about 10%, the maximum values of w_{rms} (Fig. 3(c)) and v_{rms} (Fig. 3(d)) while the results of LES using the same grid resolution ($81 \times 81 \times 31$) agree well with DNS of Woerner (1994) obtained with a much finer grid ($200 \times 200 \times 49$). From this validation exercise it can be concluded that present LES of turbulent Rayleigh–Bénard flows with relatively moderate grid resolutions are able to correctly predict the main statistics of the flow.

4. Results and discussion

The perfectly conducting Rayleigh–Bénard cell (i.e. fixed linear vertical temperature distribution on the four lateral walls) allows heat transfer between the sidewalls and the convecting fluid. Local and average heat transfer rates, integrated over the whole surface (S) of a particular wall (w), are defined in Eqs. (5) and (6), respectively.

$$\vec{q}_{\mathrm{w}} = -\left.\frac{\partial T}{\partial x_n}\right|_{\mathrm{w}} \vec{n}, \tag{5}$$

$$\bar{q}_{\mathrm{w}} = \frac{1}{S}\int_S q_{\mathrm{w}}\,\mathrm{d}S, \tag{6}$$

where x_n and n are the coordinate and the unit vector perpendicular to the wall, respectively. According to the definition of q_{w} in Eq. (6), negative values of local heat transfer indicate output of thermal energy from the fluid to the walls while positive values of q_{w} imply heat transfer from the solid boundary to the convecting fluid. Note that, by definition, q_{w} integrated over the surface of the six walls of the cavity is zero for a steady time-averaged flow. The local Nusselt number can be obtained taking the absolute value of q_{w}.

4.1. Laminar flow structures at $Ra \leqslant 10^5$

Numerical results of flows ($Pr = 0.71$) in a cubical cell with adiabatic lateral walls, reported in Pallares et al. (1999), were used as initial conditions for the simulations in the perfectly conducting cavity at low Rayleigh numbers ($Ra = 4 \times 10^4$ for S1 and S5) and ($Ra = 6 \times 10^4$ for S3). In the present study, the flow and thermal fields at a given Rayleigh number in a perfectly conducting cavity were successively used as initial conditions for other values of the Rayleigh number. While for the adiabatic case up to seven different flow structures were seen to be stable (see Fig. 1), in the present work, focused on a cavity with perfectly conducting walls, only structures S1, S3 and S5 were obtained for $Ra \leqslant 10^5$.

Fig. 4 shows the distributions of the local heat transfer rates, q_{w}, for structure S1 at $Ra = 4 \times 10^4$, and structures S3 and S5 at $Ra = 8 \times 10^4$ in a perfectly conducting cavity. Contours on the walls $x = 0$, $y = 0$ and $z = 0$ are shown in Fig. 4(a), (c) and (e) and contours on the other three walls, $x = L$, $y = L$ and $z = L$ are depicted in Fig. 4(b), (d) and (f). The extreme values of q_{w} on the horizontal walls are caused by flow impingement, hotter or colder than the wall. Correspondingly, low absolute values indicate thermal boundary layer development. Hot-ascending/cold-descending motions occurring near the sidewalls of the cavity produce regions of negative/positive q_{w} on the lateral walls.

Fig. 4(a)–(d) show that the single roll structures S1 and S3, with the axis of rotation parallel to the x-direction, produce two symmetrically distributed flow impingements on each horizontal wall. The distance between the positions of the maximum heat transfer rates is the same on both horizontal walls for structure S1. On the other hand, the flow impingements generated

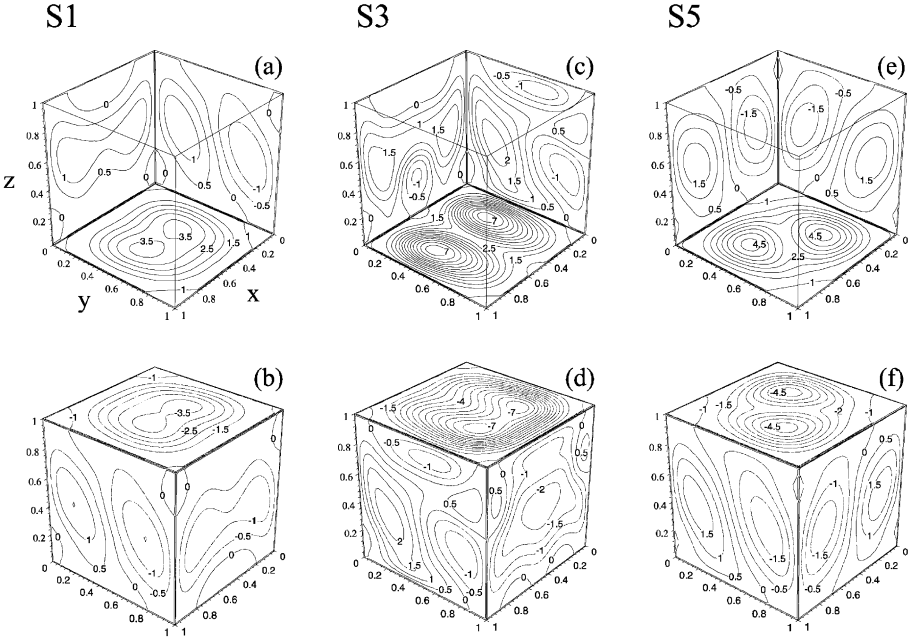

Fig. 4. Local heat transfer rates on the six walls of a perfectly conducting cavity generated by (a and b) structure S1 at $Ra = 4 \times 10^4$, (c and d) structure S3 at $Ra = 8 \times 10^4$ and (e and f) structure S5 at $Ra = 8 \times 10^4$. Negative values of q_{w} are indicated with dotted lines. The contour increment in all the figures is 0.5.

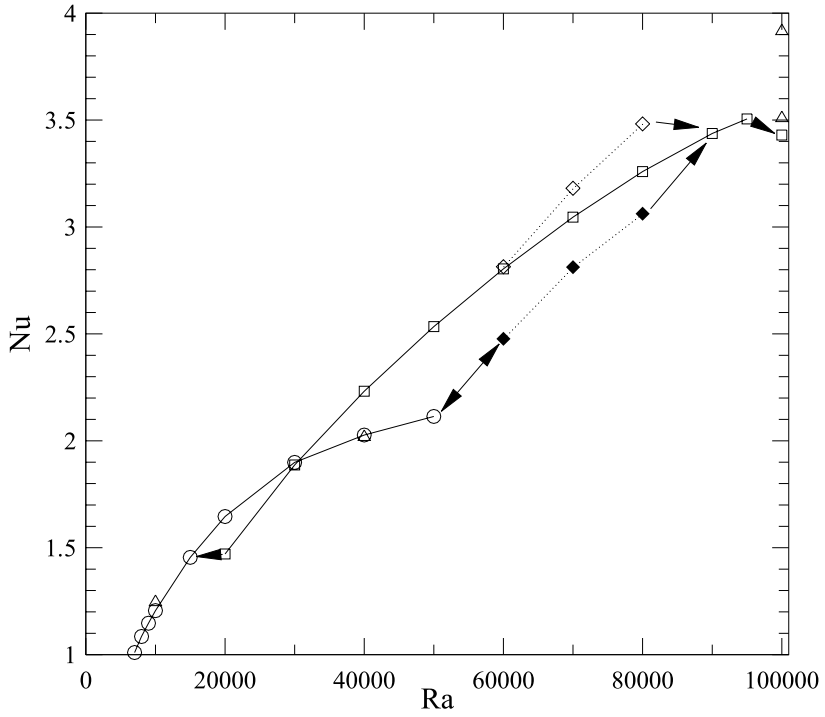

Fig. 5. Average Nusselt numbers on the horizontal plates. (a) Low Rayleigh numbers. (△) Leong et al. (1999), (○) S1, (◆) S3 bottom wall, (◇) S3 top wall, (□) S5. The arrows indicate the flow transitions observed.

by structure S3 are closer on the bottom wall (Fig. 4(c)) than on the top wall (Fig. 4(d)). According to the flow topologies of these single rolling motions, reported by Pallares et al. (1999) in a cubical cavity with adiabatic lateral walls, Fig. 4(a) and (b) show that structure S1 generates antisymmetric distributions of q_w on the horizontal and lateral walls $y = 0$ and 1. As shown in Fig. 4(c), structure S3 generates two descending main currents near the vertical edges $x = 0$, $y = 0$ and $x = 1$, $y = 0$ which produce two separated local maxima of q_w on the wall $y = 0$. The main ascending flow occurs near the wall $y = 1$ and generates a single maximum of q_w on this wall. The flow circulation in structure S3 produces different average heat transfer rates on the horizontal walls and on the vertical walls parallel to the rotation axis. The distributions of the local heat transfer rates of the four-roll structure S5 (Fig. 4(e) and (f)) show that ascending currents occur near the vertical edges $x = 1$, $y = 0$ and $x = 0$, $y = 1$ and that descending flows occur near the other two vertical edges of the cavity (see Fig. 1). As shown in Fig. 4(e) and (f) the impingements of the vertical currents on the horizontal walls produce two diagonally distributed maxima of q_w.

Fig. 5 shows the average Nusselt numbers on the horizontal plates of the flow structures (S1, S3 and S5) at $Ra \leqslant 10^5$. In the case of structures S1 and S5 the average Nusselt numbers at the hot wall is identical to the value obtained at the cold wall while structure S3 generates different average heat transfer rates at the two horizontal plates. The different averaged heat transfer rates at the bottom and top cold walls produced by structure S3 are plotted in the range of Rayleigh numbers in which this structure was found to be stable. For purposes of comparison, Fig. 5 also shows the measurements reported by Leong et al. (1999). The extrapolation of the Nu vs. Ra curve at $Nu = 1$ predicts a critical Rayleigh number of $Ra_C \approx 7 \times 10^3$ in agreement with linear stability analysis (Catton, 1970; Mizushima and Matsuda, 1997) and experimental work (Leong et al., 1999). Structure S1 is obtained as a steady flow pattern in the range $7 \times 10^3 \leqslant Ra \leqslant 4 \times 10^4$. As the Rayleigh number is increased from 4×10^4 to 5×10^4 this structure evolves to an unsteady S3 structure, which was found to exist in the range $5 \times 10^4 \leqslant Ra \leqslant 6 \times 10^4$. The time evolution of this unsteady flow structure shows that the flow is oscillating with a single characteristic frequency $(f^* = 7 \times 10^{-3}(g\beta\Delta T/L)^{1/2}$ at $\mathrm{Ra} = 5 \times 10^4$ and $f^* = 10^{-2}(g\beta\Delta T/L)^{1/2}$ at $\mathrm{Ra} = 6 \times 10^4)$. At $\mathrm{Ra} = 8 \times 10^4$, a steady S3 structure is obtained when an instantaneous flow field of the oscillatory time-dependent S3 structure at $Ra = 7 \times 10^4$ is used as an initial condition. A similar atypical flow sequence, in which a non-steady flow structure reverts to a steady state when the Rayleigh number is increased, has been reported in experiments (Gollub and Benson, 1980) and numerical simulations (Mukutmoni and Yang, 1995) in rectangular small aspect ratio enclosures at $Ra \approx 10^5$ and $Pr = 5$. The S3 structure evolves to the four-roll structure S5 as

the Rayleigh number is increased from $Ra = 8 \times 10^4$ to 9×10^4. Structure S5 remains steady for $2 \times 10^4 \leqslant Ra \leqslant 9 \times 10^4$.

Differences between the Nusselt numbers measured by Leong et al. (1999) at $Ra = 10^4$ and 4×10^4 and the corresponding present predictions ($Nu = 1.18$ at $Ra = 10^4$ and $Nu = 2.03$ at $Ra = 4 \times 10^4$) are 5% and 0.6%, respectively (Fig. 5). The significant difference at $Ra = 10^4$ may be related to the different flow structure in the experiments. Experimental visualizations by Pallares et al. (2001) in a cubical cavity filled with silicone oil ($Pr = 130$) at $Ra \leqslant 10^4$ showed that the preferred flow structure under this conditions was the diagonally aligned single roll S2 (see Fig. 1). However, the diagonally aligned roll could not be stabilized in any of the present numerical simulations.

The measurements of the Nusselt numbers obtained by Leong et al. (1999) at $Ra = 10^5$ fell into two sets depending on the value of the mean temperature of their experiments. The simulations they carried out in one half of the cavity revealed that the Nusselt numbers on the horizontal walls of a S3 structure agreed with the measured values. This suggests that the variation of the physical properties with temperature may play an important role in the selection of the spatial orientation of the flow structure. In fact, Leong et al. (1999) found that the computed Nusselt number was within the experimental uncertainty if the simulations take into account the variation of the physical properties with temperature.

In contrast to the simulations of Leong et al. (1999) in one half of the cavity, present simulations of the full cavity, assuming constant fluid properties at $Ra = 10^5$, predict an unsteady S5 structure with a time-averaged Nusselt number of $Nu = 3.38$. Fig. 5 shows that the onset of unsteadiness produces a change in the slope of the Nu vs. Ra curve. The simulations carried out only in one half of the cavity at $Ra = 10^5$, using the same grid resolution ($21 \times 41 \times 41$), evolved to a time-dependent oscillatory structure S6 (see Fig. 1) with a time-averaged Nusselt numbers in the hot and cold walls of $Nu = 2.92$ and 3.61, respectively. Three different initial conditions were used to show how initial conditions can affect the flow structure selection when the simulation is restricted to one half of the cavity. All these conditions were: (1) conductive state and velocity field set to zero, (2) structure S5 at $Ra = 10^5$ and (3) structure S3 at $Ra = 8 \times 10^4$. These three different initial conditions led to the same time-dependent oscillatory S6 structure. When the computational domain was extended to the full cavity and structure S6 was set as an initial condition the simulation reverted to an S5 structure. This suggests that the preferred flow structure for the present numerical conditions at $Ra = 10^5$ ($Pr = 0.7$) is the four-roll structure S5.

4.2. Flow structures at $Ra = 10^6$ and 10^8

LESs at $Ra = 10^6$ and 10^8 were carried out using the conductive state as initial condition. Table 3 shows some time and volume averaged quantities of the flow. The flow statistics discussed in this section were obtained by sampling the fully developed grid-resolved velocity and thermal fields during 176 ($Ra = 10^6$) and 168 ($Ra = 10^8$) non-dimensional time units. It can be seen in Table 3 that the time and volume averaged value of the rms of the velocity components, $(2\langle K\rangle_V)^{1/2}$, is about 150% of the averaged modulus of the velocity vector, $\langle|\vec{V}|\rangle_V$, indicating that the flow at $Ra = 10^6$ and $Ra = 10^8$ presents large fluctuation intensities with respect to the corresponding time-averaged flow topologies. Considering the averaged modulus of the velocity vector as a typical velocity scale of the flow, the distance covered by a fluid particle during the sampling time is about 14 times the cavity height. The averaged values of the ratio between the SGS viscosity and the molecular viscosity are 0.5% at $Ra = 10^6$ and 8% at $Ra = 10^8$. However, maximum instantaneous values of this ratio attain 5% ($Ra = 10^6$) and 100% ($Ra = 10^8$) during the simulations. The small SGS contribution at $Ra = 10^6$ indicates that the grid resolution used (61^3) captures most of the small structures of the flow and consequently, the simulation is fairly close to a DNS.

Following the method proposed by Jeong and Hussain (1995) to detect the occurrence of vortex cores, Fig. 6(a-1) ($Ra = 10^6$) and Fig. 6(b-1) ($Ra = 10^8$) show the time-averaged three-dimensional flow topologies in terms of a surface of constant negative value of λ_2, the second largest eigenvalue of the velocity gradient tensor. More details about this definition can be found in Jeong and Hussain (1995). The time-averaged vector fields and the rms contours in the vertical planes indicated in Fig. 6(a-1) and Fig. 6(b-1) are shown in Fig. 6(a-2) and (a-3) ($Ra = 10^6$) and Fig. 6(b-2) and (b-3) ($Ra = 10^8$). For clarity, in Fig. 6(b-2) and (b-3) ($Ra = 10^8$), only half of the vectors in each direction are plotted. The

Table 3
Volume averaged quantities and averaged Nusselt numbers at $Ra = 10^6$ and 10^8 ($Pr = 0.7$)

	Leong et al. (1999)	Present study						
Ra	Nu	t_s	$\sqrt{2\langle K\rangle_V}$	$\langle\|\vec{V}\|\rangle_V$	$\langle T_{rms}\rangle_V$	$\langle v_{SGS}\rangle_V/v$ (%)	Nu_{rms}	Nu
10^6	7.88 ± 0.09	176	0.12	0.085	0.070	0.5	0.37	7.5 ± 0.05
10^8	31.2 ± 0.4	168	0.14	0.086	0.053	8	1.5	36.5 ± 0.1

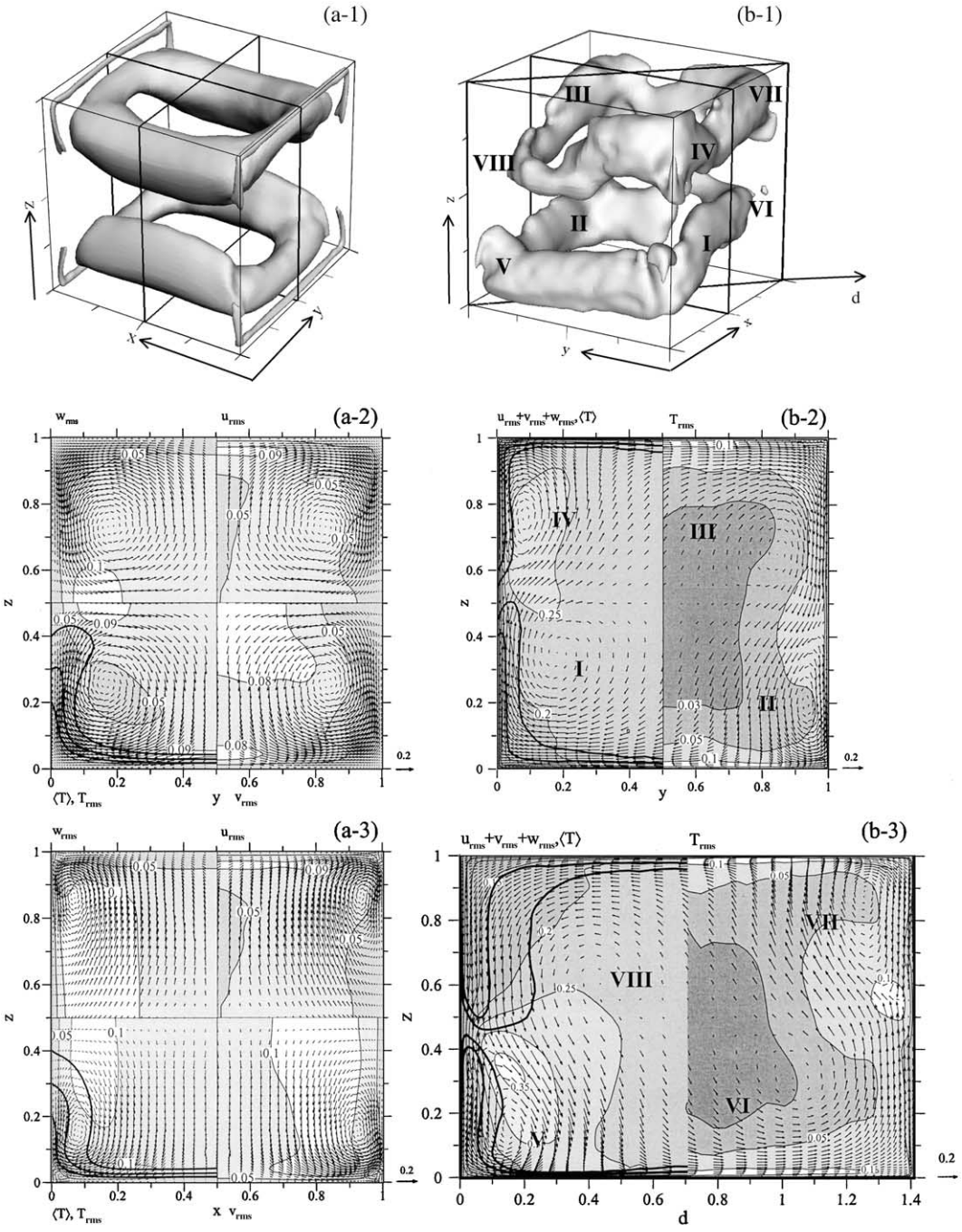

Fig. 6. Time averaged flow fields at (a) $Ra = 10^6$ and (b) $Ra = 10^8$. ((a-1) and (b-1)) Surfaces of constant value of λ_2, $\lambda_2/|\lambda_2|_{\min} = -0.1$. ((a-2) and (a-3)) Averaged vector fields, thick line contours of averaged temperature and filled contours of the fluctuation intensities in the vertical planes $x = 0.5$ and $y = 0.5$. ((b-2) and (b-3)) Thick line temperature contours and filled contours of the fluctuation intensities in the plane $x = 0.5$ and the diagonal symmetry plane. The values of the temperature contours are $\langle T \rangle = 0.1$, 0.2 and 0.3 in (a-2) and (a-3) and $\langle T \rangle = -0.05$, -0.1, 0.05 and 0.1 in (b-2) and (b-3). The vector near the bottom right corner of (a-2) to (b-3) shows the scale of the velocity vectors plotted.

irregularities on the surface of λ_2, corresponding to $Ra = 10^8$ (Fig. 6(b-1)), can be attributed to insufficient sampling time to compute the flow statistics. Table 3 shows that the rms of the averaged Nusselt on the horizontal walls at $Ra = 10^8$ is about 4.5 times the one at $Ra = 10^6$ while the sampling time (t_s) is 4% lower (see Table 3). The sampling time used at $Ra = 10^8$ falls in the limit of the computational capabilities of the present study requiring about 40 days of CPU time to obtain an averaged field. The time-averaged Nusselt numbers at $Ra = 10^6$ and 10^8 are shown in Table 3 together with the root mean-square error due to the finite integration time (Tennekes and Lumley, 1992). The differences between the averaged Nusselt numbers on the bottom and top

walls are within this error. At $Ra = 10^8$ the sampling time, and thus the CPU time, should be, approximately, doubled to decrease a 50% the error of the time-averaged Nusselt number on the horizontal plates. Nevertheless, differences between the numerically predicted Nusselt numbers and the measurements of Leong et al. (1999), shown in Table 3, are as small as 5% at $Ra = 10^6$ and only 15% at $Ra = 10^8$.

The average flow structure at $Ra = 10^6$ consists of two main counter rotating vortex rings located near the horizontal walls and four small vortex tubes near the y-edges of the cavity (see Fig. 6(a-1)). It can be seen that the time-averaged flow topology is symmetric with respect the horizontal and vertical mid planes of the cavity. The main vortex ring structure can be understood as a combination of four x-rolls (i.e. with vorticity aligned with the x-direction) located near the x-edges of the cavity and four y-rolls near the y-edges, as can be inferred from the vector fields of Fig. 6(a-2) and (a-3) and the three-dimensional flow topology of Fig. 6(a-1). The main vortex rings generate flows from the horizontal walls towards the sidewalls and from there to the horizontal walls (Fig. 6(a-2) and (a-3)). The small four corner tubes, observed in the time-averaged flow field and located near the y-edges of the cavity, intake fluid from the vortex ring near the vertical symmetry mid plane $y = 0.5$. From there, the fluid particles in this time-averaged flow are diverted towards the sidewalls ($y = 0$ and 1) rotating about the axis of the small tubes. Close to the sidewalls, the flow from the vortex tubes is reintroduced to the main vortex rings through the bends of the vortex tubes shown in Fig. 6(a-1).

Fig. 7(a) shows an instantaneous flow field at $Ra = 10^6$ in terms of isosurfaces of the vertical velocity component, w, (Fig. 7(a-1)) and vector fields in planes $x = 0.25$ and 0.75 (Fig. 7(a-2)) and $y = 0.25$ and 0.75 (Fig. 7(a-3)). Note that Fig. 7 only serves as an example of a typical state of the flow. It can be seen in Fig. 7(a) that the confining effect of the sidewalls generates important ascending and descending currents near these walls. Near the horizontal mid plane $z = 0.5$, the upward and downward streams are conducted towards the

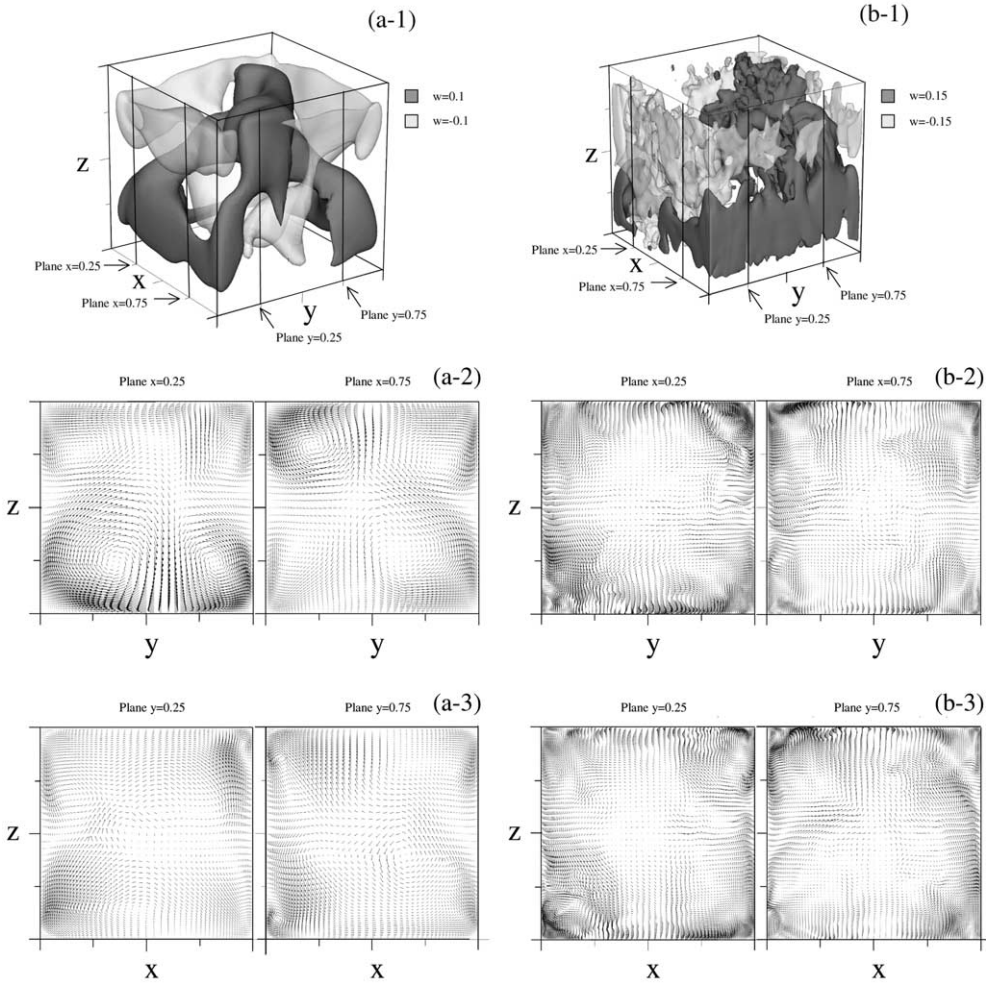

Fig. 7. Instantaneous flow visualization at (a) $Ra = 10^6$ and (b) $Ra = 10^8$. ((a-1) and (b-1)) Isosurfaces of the vertical velocity component, w. ((a-2), (a-3), (b-2) and (b-3)) Vector fields in planes $x = 0.25$, $x = 0.75$, $y = 0.25$ and $y = 0.75$.

central part of the cavity to produce impinging flow regions on the horizontal plates (see Fig. 7(a)). In Fig. 7(a-2), instantaneous x-rolls are clearly identified, near the four x-edges of the cavity. In contrast, only some of the four y-rolls near the y-edges can be seen in Fig. 7(a-3). As shown in Fig. 7(a-3) they appear together with vortical motions near the horizontal midplane of the cavity ($z = 0.5$).

Comparison of the distributions of the velocity and temperature fluctuation intensities shown in Fig. 6(a-2) and (a-3) indicates that, on average, larger flow unsteadiness occurs near the sidewalls $x = 0$ and 1 in comparison with the sidewalls $y = 0$ and 1. Obviously this corresponds to this specific realization; there is an exact equal possibility of obtaining just the opposite case. In fact, the centers of the y-rolls (Fig. 6(a-3)) are closer to the corresponding sidewalls ($x = 0$ and 1) than the x-rolls (Fig. 6(a-2)). The different fluctuation intensities near the x and y sidewalls are consistent with the instantaneous flow visualization example at $Ra = 10^6$ shown in Fig. 7(a). Also, the inspection of several snapshots of the flow indicates that the four x-rolling

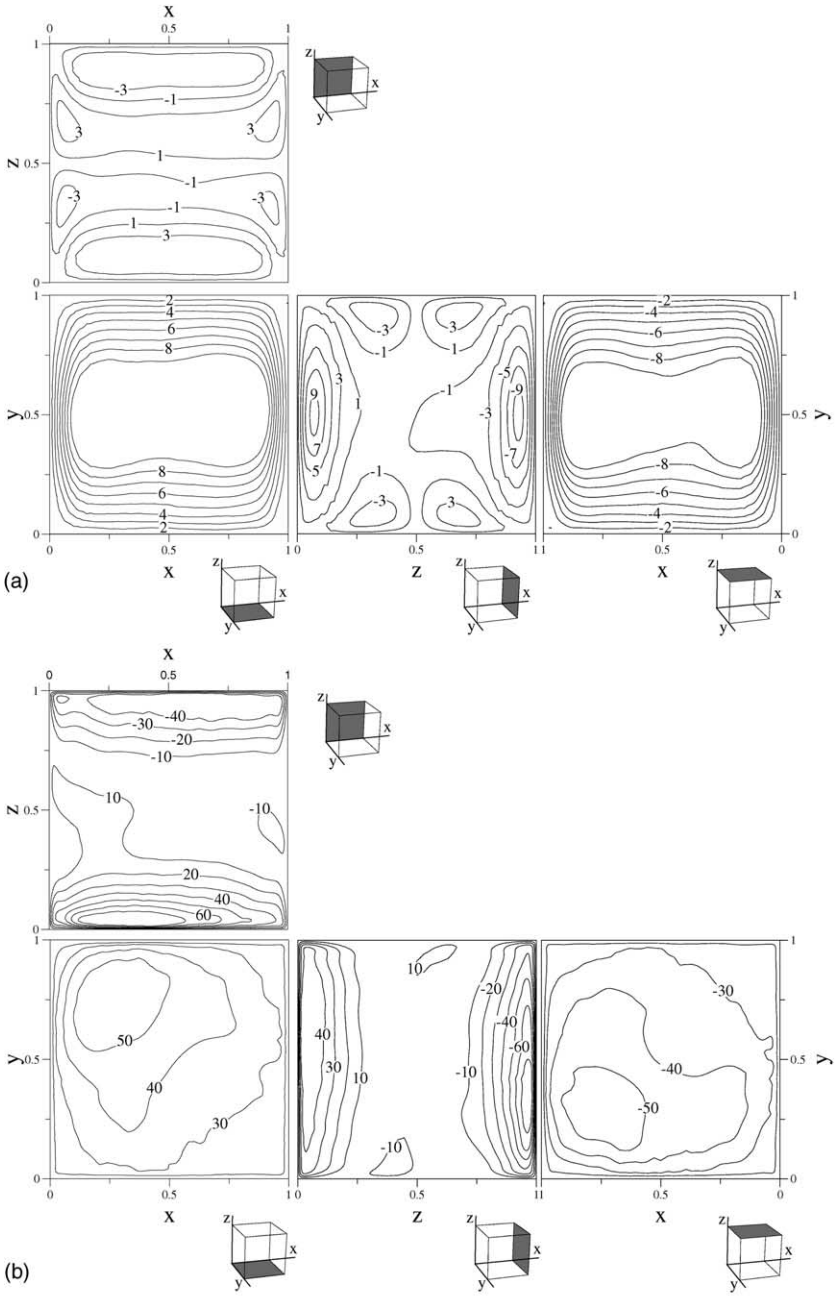

Fig. 8. Time-averaged heat transfer rates on the walls of the cavity at (a) $Ra = 10^6$ and (b) $Ra = 10^8$.

motions shown in Fig. 6(a-2) are more persistent that the y-rolls of Fig. 6(a-3). In the cross-section of the x-rolls (Fig. 6(a-2)), large fluctuation intensities are located away from the sidewalls $y = 0$ and 1, near the horizontal mid plane of the cavity $z = 0.5$, where the flow is separated from these lateral walls. Fig. 6(a-2) shows that local maxima of the rms occur near the impingement of the rolling motions on the bottom and top walls. As an example, at $x = 0.5$, $y = 0.5$ and $z = 0.05$, $u_{\mathrm{rms}} = v_{\mathrm{rms}} = T_{\mathrm{rms}} = 0.09$, $w_{\mathrm{rms}} = 0.05$, $w = 0.03$ and because of symmetry, $u = 0$ and $v = 0$.

The time-averaged distributions of the local heat transfer rates, defined in Eq. (5), on the walls of the cavity generated by the vortex ring structures at $Ra = 10^6$ are shown in Fig. 8(a). Because of the symmetry elements of the vortex ring structures, the distributions of q_{w} on the walls $x = 0$ and $z = 1$, not shown, are equivalent to the ones plotted in Fig. 8(a) at $x = 1$ and $z = 0$, respectively. It can be seen that the extreme values of heat transfer rates are located in the central region of the horizontal walls and are distributed along the y-direction according to the larger rolling motions of the y-rolls (Fig. 6(a-2)) in comparison with the x-rolls (Fig. 6(a-3)). Although the time- and surface-averaged heat transfer flux for each sidewall is zero, according to the symmetry elements of the time-averaged flow, Fig. 8(a) shows that near the horizontal walls there is significant heat transfer between the fluid and the conductive sidewalls. It can be seen in Fig. 8(a) that the flow is heated/cooled near the bottom/top part of the lateral walls. The larger extreme values of q_{w} on the sidewalls $x = 1$ and 0 in comparison with the sidewalls $y = 0$ and 1 agree with the time-averaged temperature distribution shown in the bottom left quadrant of Fig. 6(a-2) and (a-3) with thick line contours. Note that the locations of the y-rolls (Fig. 6(a-2)), closer to the corresponding horizontal edges of the cavity than the x-rolls (Fig. 6(a-3)), produce larger heat transfer rates (i.e. concentration of the temperature contours) on sidewalls $x = 0$ and 1 than in the walls $y = 0$ and 1.

Fig. 6(b-1) shows that at $Ra = 10^8$ the time-averaged vortex ring structures are detached from the horizontal walls near two diagonally opposed vertices of the cavity. The Roman numerals of Fig. 6(b-1) identify the vortex cores shown in the two vertical cuts of the flow of Fig. 6(b-2) and (b-3). It can be seen that the vector fields shown in these figures are antisymmetric with respect to the center of the cavity ($x = 0.5$, $y = 0.5$, $z = 0.5$). Consequently, the flow topology can be considered symmetric with respect to the diagonal symmetry plane of the cavity (z, d) indicated in Fig. 6(b-1).

The topology of the instantaneous flow field at $Ra = 10^8$ shown in Fig. 7(b-1)–(b-3) indicates an increase of the overall turbulence level of the flow in comparison with the large-scale and more organized motions of Fig. 7(a-2) and (a-3) at $Ra = 10^6$. Despite, the irregularities on the isosurfaces of w (Fig. 7(b-1)), produced by small-scale fluctuations, Fig. 7(b-1) shows that ascending and descending sheets of fluid occur near the sidewalls of the cavity. The instantaneous vector fields of Fig. 7(b-2) and (b-3) show that some vertical currents separate from the sidewalls. Note for example the vertical flow in Fig. 7(b-2) in the plane $x = 0.75$ near the sidewall $y = 0$. In contrast, some others flow along all the length of the lateral wall towards the horizontal walls (see for example the vertical flow in Fig. 7(b-2) in the plane $x = 0.25$ near the sidewall $y = 0$).

The comparison between the topology of the time-averaged vortex ring structures at $Ra = 10^6$, with three symmetry planes ($x = 0.5$, $y = 0.5$ and $z = 0.5$) and $Ra = 10^8$, with a diagonal symmetry plane, shows a clear symmetry reduction as the overall turbulence level of the flow is increased. The expected augmentation of the irregularity of the generation and spatial distribution of vertical currents as the turbulence level of the flow is increased would produce time-averaged flows symmetric with respect the two vertical diagonal planes of the cavity. However the symmetry reduction observed at $Ra = 10^8$ suggests a considerable organization of the generation and spatial distribution of the instantaneous ascending and descending currents, produced by the confining effect of the sidewalls.

The distributions of the velocity and temperature fluctuations intensities at $Ra = 10^8$ are shown in Fig. 6(b-2) and (b-3). Note that because of the symmetry of the time-averaged flow these distributions are symmetric with respect to the center of the cavity. It can be seen in Fig. 6(b-2) and (b-3) that, near the sidewalls, the maximum temperature and velocity fluctuation intensities are located near the position on the sidewalls where the vertical currents separate from these walls. In these maxima, the vertical fluctuation intensities, w_{rms}, contributes by about a 50% to the overall rms value plotted in Fig. 6(b-2) and (b-3).

The local heat transfer rates on the walls of the cavity at $Ra = 10^8$ are plotted in Fig. 8(b). The extreme values of q_{w} on the horizontal walls are situated near two diagonally opposed vertical edges of the cavity. The positions of the maximum and minimum heat transfer rates on the bottom and top walls correspond to the position of the stagnation points on the horizontal plates of the vector field in the vertical diagonal plane shown in Fig. 6(b-3). It can be seen in Fig. 8(b) that there is significant heat transfer input or output through the lateral conductive walls of the cavity where the vortex ring structures approach the horizontal walls. This is consistent with the averaged temperature thick line contours plotted in the left part of Fig. 6(b-2), where the x-roll IV, closer to the sidewall $y = 0$ than the x-roll I, produces the concentration of the temperature contour near the lateral wall.

5. Conclusions

Laminar and turbulent Rayleigh–Bénard flows in a perfectly conducting cubical cavity were numerically simulated. Two single roll structures and one four-roll structure were found to be stable at low Rayleigh numbers ($Ra \leqslant 10^5$). In this range of Rayleigh numbers, several transitions between laminar flow structures were observed. There is a general agreement between the computed Nusselt numbers on the horizontal walls of the cavity and the measurements at $Ra = 10^4$, 4×10^4, 10^6 and 10^8 reported by Leong et al. (1999). LESs at high Rayleigh numbers ($Ra = 10^6$ and 10^8) predicted time-averaged vortex ring structures near the horizontal walls. These structures are produced by the recirculation of instantaneous large-scale persistent vertical currents ocurring near the sidewalls. The vertical motions are generated, near the horizontal walls, by the confining effect of the lateral walls and by the heat transfer between the convecting fluid and the conductive sidewalls. At $Ra = 10^6$ the vortex ring structures produce different flow topologies and fluctuation intensities near two consecutive lateral walls of the cavity. The instantaneous flow field visualizations show an organized distribution of large-scale vortical motions within the cavity. The time-averaged flow at $Ra = 10^8$ shows a diagonal orientation of the vortex ring structures and the instantaneous flow fields present small-scale fluctuations produced by the overall increase of the turbulence level of the flow in comparison with the flow at $Ra = 10^6$.

Acknowledgements

This research has been founded by the Spanish Ministry of Science and Technology under projects DPI2000-1578-C02-01 and PGC2000-2193-E.

References

Catton, I., 1970. Convection in a closed rectangular region: the onset of motion. J. Heat Transfer 92, 186–187.

Cuesta, I., 1993. Estudi numéric de fluxos laminars i turbulents en una cavitat cúbica. Ph.D thesis, Universitat Rovira i Virgili, Tarragona.

Germano, M., Piomelli, U., Moin, P., Cabot, W.H., 1991. A dynamic subgrid-scale eddy viscosity model. Phys. Fluids A 3 (7), 1760–1765.

Gollub, J.P., Benson, S.V., 1980. Many routes to turbulent convection. J. Fluid Mech. 100, 449–470.

Jeong, J., Hussain, F., 1995. On the identification of a vortex. J. Fluid Mech. 285, 69–80.

Kerr, R.M., 1996. Rayleigh number scaling in numerical convection. J. Fluid Mech. 310, 139–180.

Kim, W., Menon, S., 1997. Application of the localized dynamic subgrid-scale model to turbulent wall-bounded flows, AIAA Paper 97-0210. 35th Aerospace Sciences Meeting & Exhibit, Reno, NV.

Koschmieder, E.L., 1993. Cambridge Monographs on Mechanics and Applied Mathematics. In: Bénard Cells and Taylor Vortices, first ed. Cambridge University Press, Cambridge.

Leong, W.H., Hollands, K.G.T., Brunger, A.P., 1999. Experimental Nusselt numbers for a cubical-cavity benchmark problem in natural convection. Int. J. Heat Mass Transfer 42 (11), 1979–1989.

Mittal, R., Moin, P., 1997. Suitability of upwind-biased finite difference schemes for large-eddy simulation of turbulent flows. AIAA J 35, 1415–1417.

Mizushima, J., Matsuda, O., 1997. Onset of 3D thermal convection in a cubic cavity. J. Phys. Soc. Jpn. 66 (8), 2337–2341.

Mukutmoni, D., Yang, K.T., 1995. Thermal convection in small enclosures: an atypical bifurcation sequence. Int. J. Heat Mass Transfer 38 (1), 113–126.

Pallares, J., Arroyo, M.P., Grau, F.X., Giralt, F., 2001. Rayleigh–Bénard convection in a cubical cavity: experimental and numerical flow topologies. Exp. Fluids 31 (2), 208–218.

Pallares, J., Grau, F.X., Giralt, F., 1999. Flow transitions in laminar Rayleigh–Bénard convection in a cubical cavity at moderate Rayleigh numbers. Int. J. Heat Mass Transfer 42 (4), 753–770.

Peng, S.-H., Davidson, L., 1998. Comparison of subgrid-scale models in LES for turbulent convection flow with heat transfer. In: 2nd EF Conference in Turbulent heat transfer, Manchester, UK, pp. 5.24–5.35.

Tennekes, H., Lumley, J.L., 1992. In: A First Course in Turbulence. MIT Press, Cambridge, pp. 211–212.

Woerner, M., 1994. Direkte Simulation turbulenter Rayleigh–Bénard Konvektion in fluessigem Natrium. Ph.D thesis, University of Karlsruhe, KfK 5228, Kernforschungszentrum Karlsruhe.